Crystal Structures and Topological Aspects of the High-Temperature Phases and Decomposition Products of the Alkali-Metal Oxalates $M_2[C_2O_4]$ (M = K, Rb, Cs)

Robert E. Dinnebier,*[a] Sascha Vensky,[a] Martin Jansen,*[a] and Jonathan C. Hanson[b]

Abstract: The high-temperature phases of the alkali-metal oxalates $M_2[C_2O_4]$ (M = K, Rb, Cs), and their decomposition products $M_2[CO_3]$ (M = K, Rb, Cs), were investigated by fast, angle-dispersive X-ray powder diffraction with an image-plate detector, and also by simultaneous differential thermal analysis (DTA)/thermogravimetric analysis (TGA)/mass spectrometry (MS) and differential scanning calorimetry (DSC) techniques. The following phases, in order of decreasing temperature, were observed and crystallographically characterized (an asterisk denotes a previously unknown modification): *α-$K_2[C_2O_4]$, *α-$Rb_2[C_2O_4]$, *α-$Cs_2[C_2O_4]$, α-$K_2[CO_3]$, *α-$Rb_2[CO_3]$, and *α-$Cs_2[CO_3]$ in space group $P6_3/mmc$; *β-$Rb_2[C_2O_4]$, *β-$Cs_2[C_2O_4]$, *β-$Rb_2[CO_3]$, and *β-$Cs_2[CO_3]$ in *Pnma*; γ-$Rb_2[C_2O_4]$, γ-$Cs[C_2O_4]$, γ-$Rb_2[CO_3]$, and γ-$Cs_2[CO_3]$ in $P2_1/c$; and δ-$K_2[C_2O_4]$ and δ-$Rb_2[C_2O_4]$ in *Pbam*. With respect to the centers of gravity of the oxalate and carbonate anions, respectively, the crystal structures of all known alkali-metal oxalates and carbonates belong to the AlB_2 family, and adopt either the AlB_2 or the Ni_2In arrangement depending on the size of the cation and the temperature. Despite the different sizes and constitutions of the carbonate and oxalate anions, the high-temperature phases of the alkali-metal carbonates $M_2[CO_3]$ (M = K, Rb, Cs), exhibit the same sequence of basic structures as the corresponding alkali-metal oxalates. The topological aspects and order–disorder phenomena at elevated temperature are discussed.

Keywords: alkali metal carbonate · alkali metal oxalate · crystal structure · oxalates · phase transitions · solid-state structures · X-ray diffraction

Introduction

Metal oxalates form an extended class of inorganic compounds that are of significant relevance in both chemistry and biology. In particular, in solid-state synthesis they are widely employed as versatile precursors for the preparation of multinary oxides along all-solid-state routes.[1–5] Two approaches are commonly used: either individual oxalates or mixtures of oxalates and oxides are decomposed thermally under mild conditions, thus providing particularly reactive binary oxides that can serve as reactants for solid-state synthesis, or various alternative precursors are treated directly with oxalates to yield the desired multinary oxide. In either case it would be highly desirable to know the conditions under which the decompositions occur and the structural evolutions during the course of the transformations to the corresponding intermediate carbonates, or oxides, respectively. In this context, anhydrous alkali-metal oxalates can serve as a source for highly reactive carbonates, which can be utilized as sources of basic oxides for the synthesis of alkali-metal oxometalates.

Until recently, only the crystal structures of $Li_2[C_2O_4]$[6] and $Na_2[C_2O_4]$[7,8] at room temperature had been published. In 2003 we reported the crystal structures of $K_2[C_2O_4]$, $Rb_2[C_2O_4]$, and $Cs_2[C_2O_4]$ under ambient conditions, as determined by X-ray powder diffraction.[9] Our investigation resulted in the first example of a staggered oxalate anion in the solid state, in $Cs_2[C_2O_4]$ and in one of the two polymorphs of $Rb_2[C_2O_4]$.

Research has also been conducted on the thermal behavior and decomposition of lithium,[10] potassium,[11,12] rubidi-

[a] Priv.-Doz. Dr. R. E. Dinnebier, Dr. S. Vensky, Prof. Dr. Dr. h.c. M. Jansen
Max-Planck-Institute for Solid State Research
Heisenbergstrasse 1, 70569 Stuttgart (Germany)
Fax: (+49) 711-689-1502
E-mail: r.dinnebier@fkf.mpg.de
m.jansen@fkf.mpg.de

[b] Dr. J. C. Hanson
Chemistry Department, Brookhaven National Laboratory
Upton, NY 11973 (USA)

Supporting information for this article is available on the WWW under http://www.chemeurj.org/ or from the author.

 DOI: 10.1002/chem.200400616 © 2005 Wiley-VCH Verlag GmbH & Co. KGaA, Weinheim

um, and cesium oxalates[13,14] using differential thermal analysis (DTA) and differential scanning calorimetry (DSC) techniques. While no phase transition was found for lithium oxalate up to its decomposition temperature, several transformations were reported for the higher homologues (see Table 1 for the transition temperatures). An additional phase transition was reported for potassium oxalate at a temperature of around 480 K upon cooling.[11] While the thermal degradation of oxalates has been studied extensively by thermo-analytical techniques,[15–18] the concomitant structural transformations have remained essentially unexplored, and no crystal structures of the high-temperature phases of the oxalates have been published. Here we report systematic, in situ studies, by powder diffraction using synchrotron radiation and thermal analysis, on the response of potassium, rubidium, and cesium oxalates to heating.

Table 1. Comparison of the DTA/DSC temperatures (in K) for phase transitions and decomposition of $M_2[C_2O_4]$ (M = K, Rb, Cs), with literature values. The temperature data from this work correspond to the onset values. For the determination of the decomposition points, the TGA curves (293–1273 K) were used, whereas for the phase transitions the DTA curves were used (293–773 K).

	δ	→γ	→β	→α	Decomp	Method	Heating rate [K min^{-1}]	Ref.
				644	800	DTA	10	
$K_2[C_2O_4]$	295	–	–	662	–	DSC	5	
				654	699	DTA	2,5	[11,12]
		497	623	629	781	DTA	10	
		522	647	660	–	DSC	5	
$Rb_2[C_2O_4]$	295							
		–	653	661	723	DTA	10	[14]
		–	–	–	748	DTA	5	[13]
			645	690	780	DTA	10	
$Cs_2[C_2O_4]$	–	295						
			661	718	–	DSC	5	
			673	724	743	DTA	10	[14]
					748–753	DTA	5	[13]

Results and Discussion

The phase transitions and the decomposition of anhydrous potassium, rubidium, and cesium oxalate were monitored in situ with synchrotron radiation in the temperature range from room temperature up to 900 K at ambient pressure, and by simultaneous thermal analysis (DTA/TGA/MS) as well as DSC. The previously reported phase transitions, found by using DTA and DSC techniques,[11–14] were confirmed by X-ray powder diffraction. The thermal analyses for potassium, rubidium, and cesium oxalate show that the decomposition of the compounds to the corresponding carbonate phases occurs in a narrow temperature range between 780 and 800 K with generation of carbon monoxide and of the secondary products carbon dioxide and oxygen. The mass loss for potassium oxalate is 16.6% (calcd 16.9%); it is 10.1% (10.8%) for rubidium oxalate and 7.8% (7.9%) for cesium oxalate. The decomposition of the corresponding carbonates is observed to start at a temperature of between 1150 and 1200 K. Endothermal peaks in the DTA and DSC data indicate several phase transitions of the alkali-metal oxalates (see Figure 1 and Table 1). Only the first phase transition (δ to γ) of rubidium oxalate has not been mentioned in the literature before, while a previously reported transition of potassium oxalate, which was only observed during a cooling cycle,[11] could not be confirmed by us. The broad, first peak in the first heating cycle (DSC) of rubidium oxalate corresponds to the decomposition of a small amount of rubidium oxalate hydrate.

The nomenclature of the phases was chosen in such a way that the aristotype in space group *P6₃/mmc*, which is found for all investigated alkali-metal oxalates and carbonates, is denoted the α-phase. All phases occurring upon cooling are given consecutive Greek letters in the order they appear, with the condition that structurally related phases of different compounds receive the same letter (Table 2). For consistency, the previously found α (*P2₁/c*) and β (*Pbam*) polymorphs of rubidium oxalate are renamed (α to γ and β to δ).[9]

Table 2. Nomenclature used throughout this paper for the different room- and high-temperature phases of $M_2[C_2O_4]$ and $M_2[CO_3]$ (M = K, Rb, Cs), based on the observed structure type.

	α	β	γ	δ
$K_2[CO_3]$	*P6₃/mmc*	*C2/c*	*P2₁/c*	–
$Rb_2[CO_3]$	*P6₃/mmc*	*Pnma*	*P2₁/c*	–
$Cs_2[CO_3]$	*P6₃/mmc*	*Pnma*	*P2₁/c*	–
$K_2[C_2O_4]$	*P6₃/mmc*	*Pnma*	*P2₁/c*	*Pbam*
$Rb_2[C_2O_4]$	*P6₃/mmc*	*Pnma*	*P2₁/c*	*Pbam*
$Cs_2[C_2O_4]$	*P6₃/mmc*	*Pnma*	*P2₁/c*	–

In the course of the preparation of anhydrous rubidium oxalate, the monoclinic γ-phase, which is metastable under ambient conditions relative to the orthorhombic δ-phase, is frozen-in. As a result, freshly prepared rubidium oxalate consists of a mixture of both polymorphs, while heating above, or storing at, room temperature leads to a complete phase transition into the orthorhombic form, which is stable at room temperature.

During the in situ synchrotron powder diffraction experiments, potassium, rubidium, and cesium oxalate were first heated until complete decomposition into the corresponding high-temperature carbonate phases had occurred. In agreement with the DSC data, one phase transition for potassium oxalate (δ→α), three phase transitions for rubidium oxalate (δ→γ→β→α), and two phase transitions for cesium oxalate (γ→β→α) were observed. Subsequently, the decomposition products rubidium and cesium carbonate were also monitored by X-ray diffraction upon cooling. Upon cooling to room temperature two phase transitions (α→β→γ) each

© 2005 Wiley-VCH Verlag GmbH & Co. KGaA, Weinheim

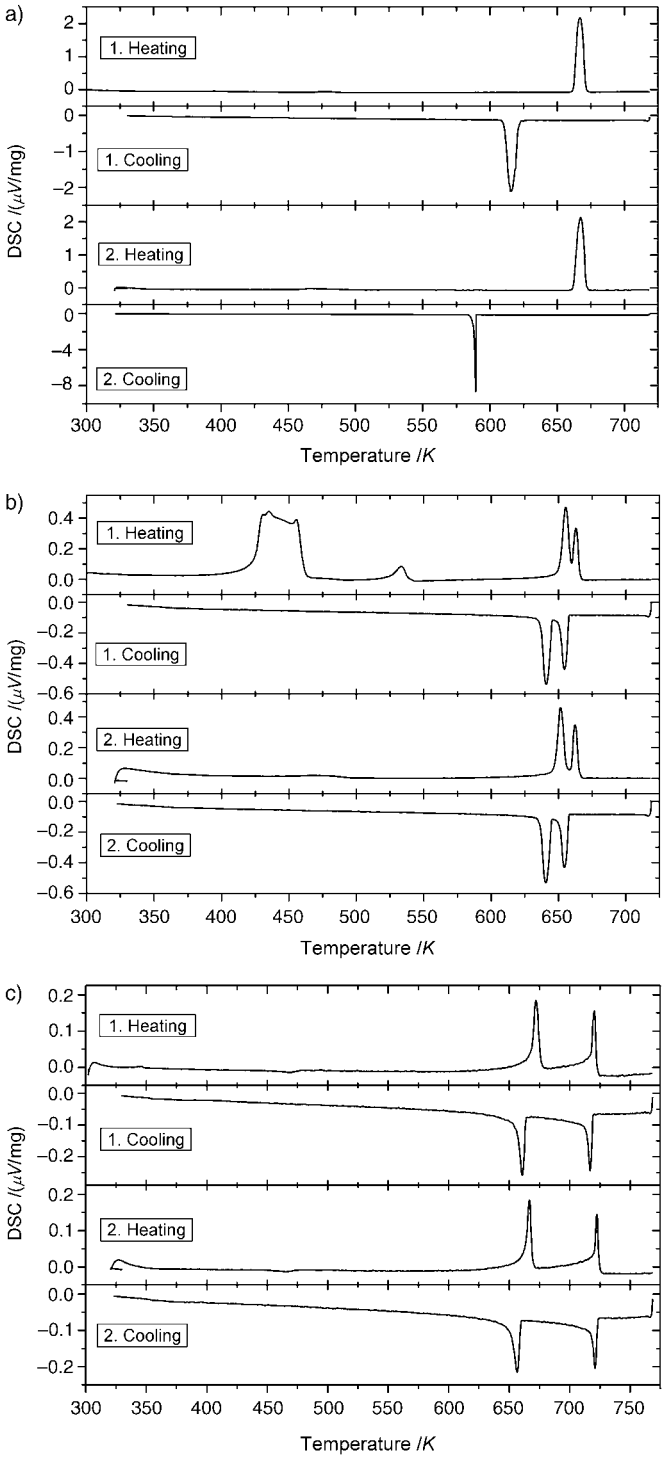

Figure 1. Differential scanning calorimetry (DSC) data for a) $K_2[C_2O_4]$, b) $Rb_2[C_2O_4]$, and c) $Cs_2[C_2O_4]$. Two consecutive heating/cooling cycles with a heating/cooling rate of 5 K min^{-1} are shown.

were observed for rubidium and cesium carbonate. For potassium carbonate, the room- (γ) and the two high-temperature phases (β and α) were already known.[19–21] The dependence of the lattice parameters on temperature and the range of existence of the different alkali-metal oxalate and carbonate phases are given in Figure 2, Figure 3, and Figure 4 for K, Cs, and Rb, respectively.

In DSC, a large hysteresis was observed for the phase transition from the δ- to the α-phase of potassium oxalate (Figure 1). This was confirmed by monitoring the change in

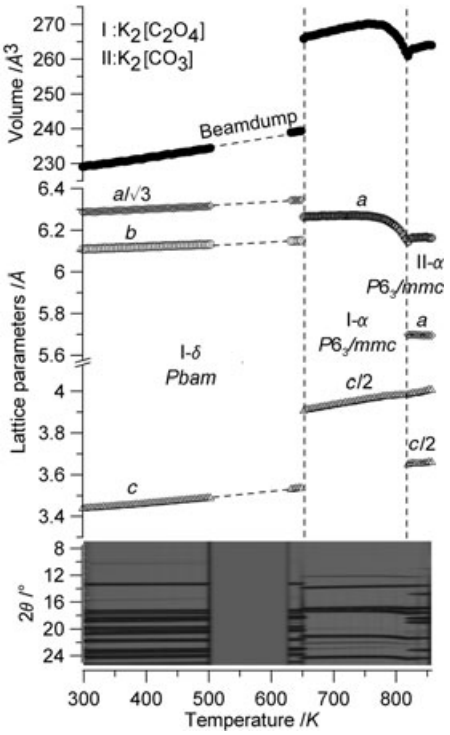

Figure 2. Powder diffraction patterns, lattice parameters, and cell volumes of $K_2[C_2O_4]$ and $K_2[CO_3]$ as a function of temperature in the range from 298 K to 856 K (1.8 K min^{-1}).

lattice parameters by in situ powder diffraction in an additional heating–cooling experiment with a maximum temperature well below the decomposition temperature (Figure 5). This behavior indicates a kinetically inhibited process with a high activation energy, which is supported by the fact that no intermediate β- and γ-phases, as in the cases of the rubidium and cesium oxalates, occur.

None of the literature values for the unit-cell parameters of high-temperature phases of potassium, rubidium, and cesium oxalate have been confirmed.[11,13,14]

The previously unknown crystal structures of α-$K_2[C_2O_4]$, α-$Rb_2[C_2O_4]$, α-$Cs_2[C_2O_4]$, α-$Rb_2[CO_3]$, α-$Cs_2[CO_3]$, β-$Rb_2[C_2O_4]$, β-$Cs_2[C_2O_4]$, β-Rb_2CO_3, and β-$Cs_2[CO_3]$ (see Table 3 and Table 4), as well as the previously reported crystal structures of γ-$Rb_2[C_2O_4]$, γ-$Cs[C_2O_4]$, γ-$Rb_2[CO_3]$, γ-$Cs_2[CO_3]$, δ-$K_2[C_2O_4]$, and δ-$Rb_2[C_2O_4]$, were solved and/or refined from the powder-diffraction data (see Figure 6, Figure 7, and Table 5). With respect to the lower data quality, only LeBail-type fits were performed for the different phases of cesium carbonate, but the similarity of the powder patterns to those of the rubidium carbonate phases led us to the conclusion that the α-, β-, and γ-phases of $Rb_2[CO_3]$ and $Cs_2[CO_3]$ are isostructural.

 © 2005 Wiley-VCH Verlag GmbH & Co. KGaA, Weinheim

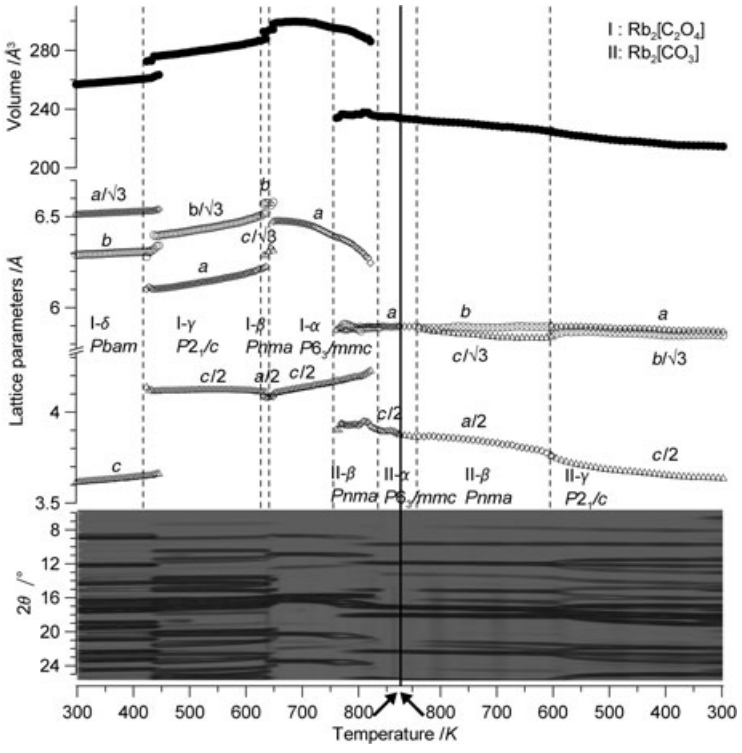

Figure 3. Powder diffraction patterns, lattice parameters, and cell volumes of $Rb_2[C_2O_4]$ and $Rb_2[CO_3]$ as a function of temperature in the range from 298 to 838 K (2.4 K min^{-1}) and back down to 298 K (4.8 K min^{-1}).

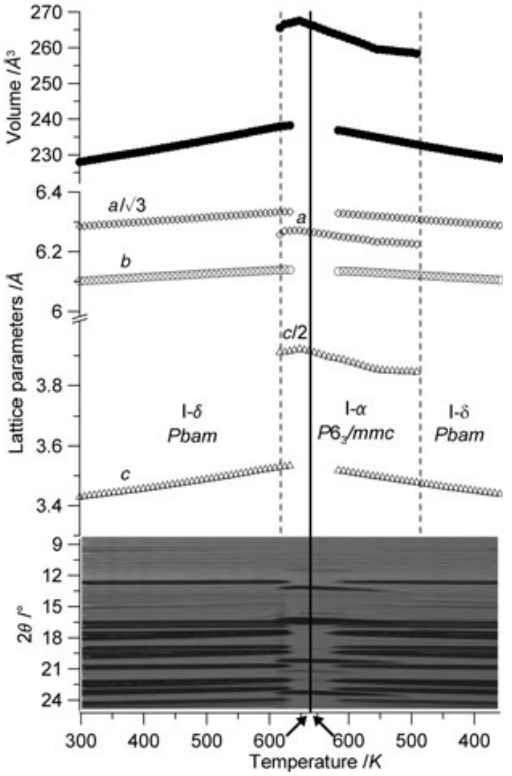

Figure 5. Powder diffraction patterns, lattice parameters, and cell volumes of $K_2[C_2O_4]$ as a function of temperature in the temperature range from 298 to 655 K (2.3 K min^{-1}) and back down to 360 K (2.3 K min^{-1}).

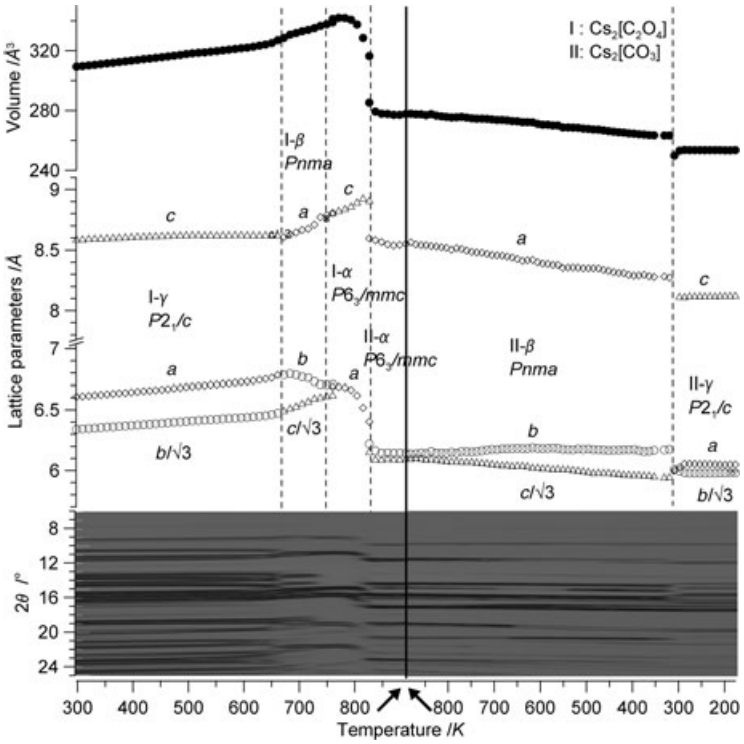

Figure 4. Powder diffraction patterns, lattice parameters, and cell volumes of $Cs_2[C_2O_4]$ and $Cs_2[CO_3]$ as a function of temperature in the range from 298 to 892 K (2.7 K min^{-1}) and back down to 298 K (2.7 K min^{-1}).

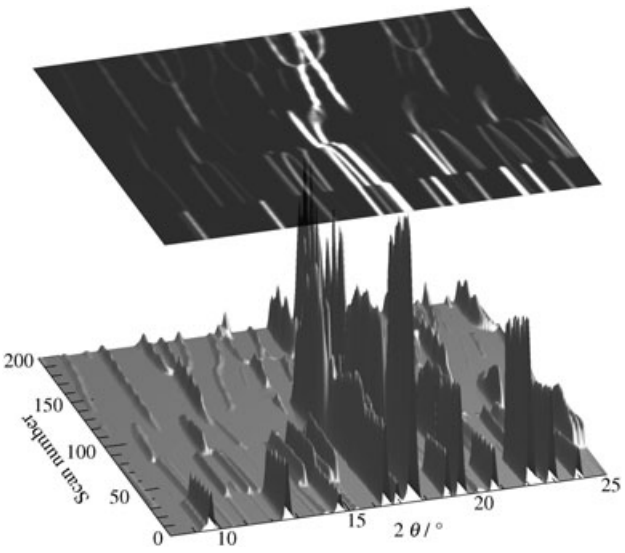

Figure 6. Three-dimensional representation and two-dimensional projection ("simulated heating-Guinier pattern") of the observed scattered X-ray intensity (z axis) for $Rb_2[C_2O_4]$ as a function of diffraction angle 2θ (x axis, 8–25° 2θ) and scan number (y axis, 1–200). The temperature range is from 298 to 873 K (2.4 K min^{-1}; scans 1–133) and back down to 298 K (4.8 K min^{-1}; scans 134–200). The wavelength was 0.9224 Å. This figure was prepared with Powder3D.[42]

© 2005 Wiley-VCH Verlag GmbH & Co. KGaA, Weinheim

Table 3. Crystallographic data for refined high-temperature alkali-metal oxalate phases. R_p and R_{wp} refer to the Rietveld criteria[41] of fit for profile and weighted profile respectively.[33]

	β-$Rb_2[C_2O_4]$	β-$Cs_2[C_2O_4]$	α-$K_2[C_2O_4]$	α-$Rb_2[C_2O_4]$	α-$Cs_2[C_2O_4]$
space group	*Pnma*	*Pnma*	*P6₃/mmc*	*P6₃/mmc*	*P6₃/mmc*
Z	4	4	2	2	2
a [Å]	8.1647(7)	8.6378(4)	6.2643(1)	6.47255 (8)	6.6333(1)
b [Å]	6.5809(6)	6.7824(3)	$=a$	$=a$	$=a$
c [Å]	10.9325(8)	11.2733(4)	7.9281(2)	8.2612(2)	8.8411(2)
temperature [*K*]	640	701	752	683	807
R_p [%]	4.15	1.71	0.81	1.70	0.90
R_{wp} [%]	6.71	2.85	1.35	2.81	1.84
R_F^2 [%]	13.37	11.34	4.04	5.46	43.73[a]
no. of reflections	220	238	49	53	57
no. of variables	13	18	14	18	18

[a] The high Bragg *R* value is due to difficulties in the integration of the image-plate data.

Table 4. Crystallographic data for refined alkali-metal carbonate phases. R_p and R_{wp} refer to the Rietveld criteria[41] of fit for profile and weighted profile respectively.[33]

	γ-$Rb_2[CO_3]$	β-$Rb_2[CO_3]$	α-$Rb_2[CO_3]$	α-$K_2[CO_3]$
space group	*P2₁/c*	*Pnma*	*P6₃/mmc*	*P6₃/mmc*
Z	4	4	2	2
a [Å]	5.8745(2)	7.6840(4)	5.8960(1)	5.6948(9)
b [Å]	10.1290(4)	5.8912(4)	$=a$	$=a$
c [Å]	7.3073(3)	10.1437(6)	7.8026(8)	7.3301(3)
β [°]	97.292(4)	–	–	–
temperature [*K*]	385	734	860	835
R_p [%]	4.67	3.82	2.96	2.57
R_{wp} [%]	6.07	5.33	5.36	3.44
R_F^2 [%]	6.48	6.61	8.91	6.31
no. of reflections	294	210	42	84
no. of variables	45	47	10	78

Table 5. Measurement parameters of the temperature-dependent in-situ X-ray powder-diffraction experiments on potassium, rubidium, and cesium oxalate.

	$K_2[C_2O_4]$	$Rb_2[C_2O_4]$	$Cs_2[C_2O_4]$
temperature range [K]	298→655→360	298→838→298	298→892→298
	298→856	–	298→760
exposure time [s]	120	30	120
	60	–	180
development time [s]	80	80	80
total time per scan [s]	200	110	200
	140	–	260
total scan number	87	200	120
	135	–	55
heating/cooling rate	2.34/2.34	2.37/4.75	2.7/2.7
[K min^{-1}]	1.8	–	2.15
wavelength [Å]	0.9224	0.9224	0.9224
2θ range [°]	7.01–46.02	5.99–46.98	6.00–46.99
step width [°]	0.022	0.024	0.023
diameter of capillary [mm]	0.5	0.5	0.3

The crystal structures of the γ- and δ-modifications of the higher homologues of the alkali-metal oxalates have been described in detail previously;[9] for the convenience of the reader a short summary is given here. In the δ- and γ-phases, the oxalate anions can be considered static, with the oxalate anions in two different conformations: planar in the δ-phase and staggered in the γ-phase (99° for γ-$Cs_2[C_2O_4]$ and 94° for γ-$Rb_2[C_2O_4]$). The layered crystal structures of the δ-modification of potassium and rubidium oxalate contain alternating layers of planar oxalate anions and alkali-metal cations. The oxalate anions form infinite parallel chains along the *c* direction, with the length of the *c*-axis as spacer. The C–C bonds of the oxalate molecules are alternately inclined by approximately ±20° relative to the *a* axis, which leads to a herringbone arrangement (Figure 8a). Each alkali-metal cation is surrounded by eight oxygen atoms in the form of a distorted cube. Two cubes form a pair through a common face, and these pairs are stacked to form infinite chains along the *c* axis.

In contrast, the crystal structures of the γ-modification of rubidium and cesium oxalate are framework structures (Figure 8b). Each of the two crystallographically different alkali-metal cations is surrounded by a different number of oxygen atoms to form irregular polyhedra. The alkali-metal atoms Cs(1) and Rb(1) are each coordinated to nine oxygen atoms (distances 3.069(9) to 3.557(9) Å for cesium and 2.888(6) to 3.386(5) Å for rubidium), from six different oxalate anions, in the form of a distorted tetragonal antiprism that is capped at one of its trigonal planes, whereas the alkali-metal cations Cs(2) and Rb(2) are coordinated to ten oxygen atoms (distances 3.015(8) Å to 3.737(9) Å for cesium and 2.816(7) Å to 3.580(7) Å for rubidium), from only five different oxalate anions, in the form of an irregular polyhedron.

A detailed description of the coordination spheres of the alkali-metal cations in the crystal structures of the α- and β-phases of the alkali-metal oxalates is not meaningful due to the apparent disorder of the oxalate anions. Therefore, only the conformation of the oxalate anions in the different modifications and the principal packing motifs were investigated further.

In the β- and α-phases, the oxalate anions are staggered and disordered. The basic packing of the γ-phase is preserved. For the β-phase, a twofold disorder model with the

 © 2005 Wiley-VCH Verlag GmbH & Co. KGaA, Weinheim

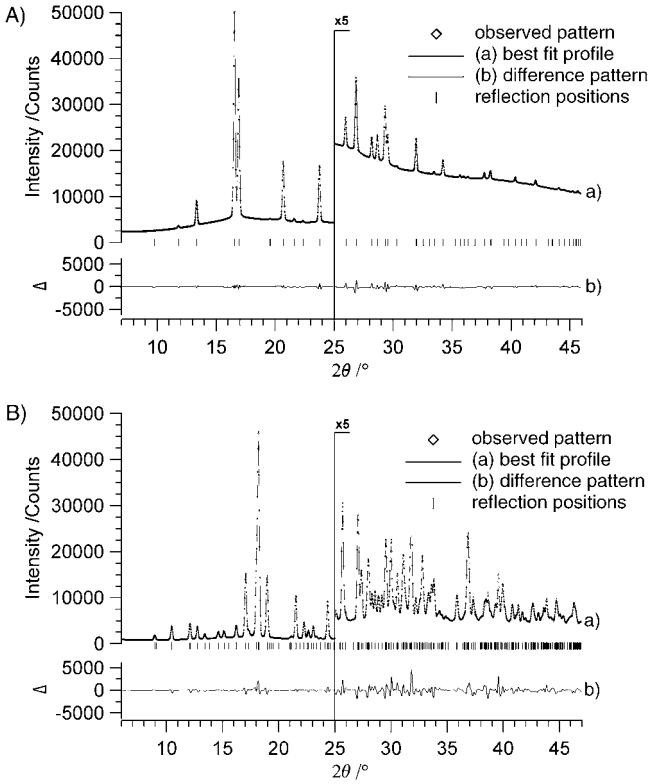

Figure 7. Scattered X-ray intensity for A) $K_2[C_2O_4]$ at 752 K and B) for $Rb_2[CO_3]$ at 385 K as a function of diffraction angle 2θ. The observed patterns (diamonds), the best Rietveld-fit profiles (line), and the difference curves between observed and calculated profiles are shown in an additional window below. The high-angle parts are enlarged by a factor of 5, starting at 25° 2θ. The wavelength was 0.9224 Å.

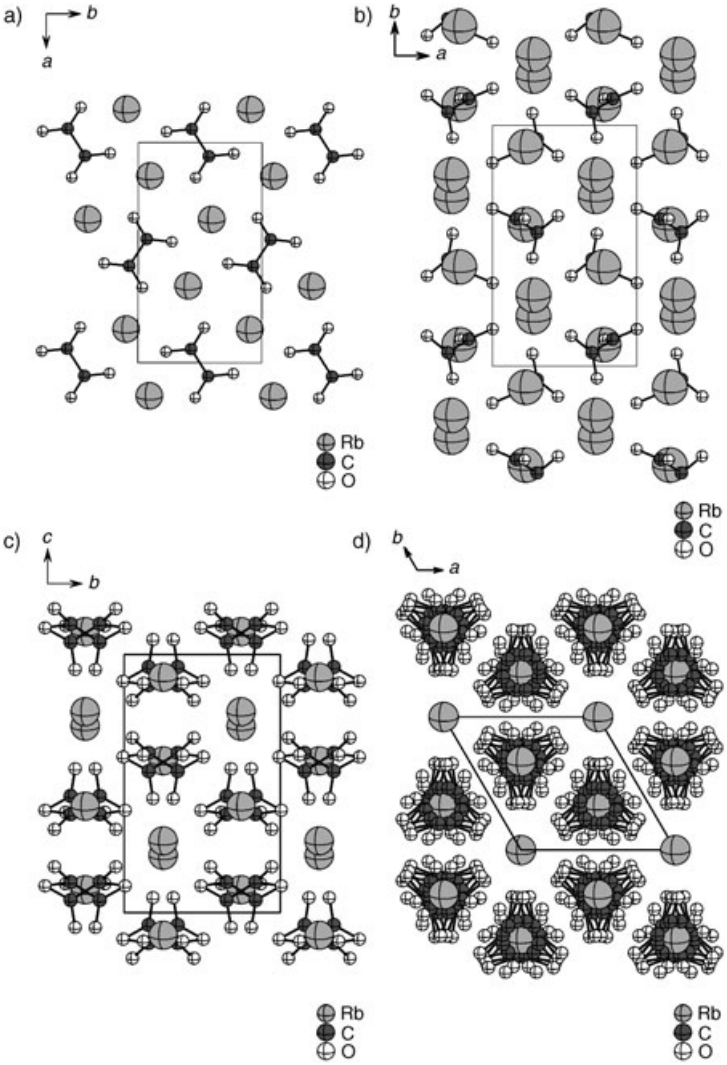

Figure 8. Ball-and-stick representation of the crystal structures of $Rb_2[C_2O_4]$: a) the orthorhombic (*Pbam*) δ-phase at 298 K in a projection down the *c* axis; b) the monoclinic ($P2_1/c$) γ-phase at 298 K in a projection down the *c* axis; c) the orthorhombic (*Pnma*) β-phase at 640 K, showing the disorder of the oxalate anions, in a projection down the *b* axis; d) the hexagonal ($P6_3/mmc$) α-phase at 683 K, showing the disorder of the oxalate anions, in a projection down the *c* axis.

oxalate anion rotating around an axis perpendicular to the principal axis proved sufficient to describe the powder-diffraction data reasonably well (Figure 8c). The disorder increases significantly for the α-phase, however. In addition to the rotation described for the β-phase, additional rotations of the carboxyl groups exist, which lead to a quasispherical entity. In this case, the powder-diffraction data suggest a 24-fold disorder model (Figure 8d). In addition, the mobility of the cations increases drastically in a nonuniform way with increasing temperature; this could be satisfactorily modeled by refining an anisotropic temperature factor.

All investigated alkali-metal carbonate phases (Figure 9) are isotypic to their corresponding alkali-metal oxalate phases given by the same phase identifier, despite the different shapes of the anions. Refinement of the crystal structure of the room temperature modification of γ-$Rb_2[CO_3]$ (and isostructural γ-$Cs_2[CO_3]$ confirmed the literature data.[22] The differences between the γ-, β-, and α-phases for potassium, rubidium, and cesium carbonate are mainly due to the different orientations of the rigid carbonate ion: whereas in the γ-modification the carbonate ions are inclined around two axes with respect to each other, they are inclined around only one axis in the β-phase because of an additional mirror plane running through the CO_3^{2-} ions. Therefore, no disorder model is necessary to match the powder-diffraction pattern of the β-modification. In β-$Rb_2[CO_3]$, and isostructural β-$Cs_2[CO_3]$, the two crystallographically independent alkali-metal cations are coordinated by a different number of oxygen atoms. While Rb(1) is coordinated by seven oxygen atoms belonging to five different carbonate anions in the form of a twofold-capped tetragonal pyramid (Rb–O distances of 2.985(7)–3.09(2) Å), Rb(2) is octahedrally coordinated by six oxygen atoms of six different carbonate anions (Rb–O distances of 2.688(3)–3.15(2) Å. The carbonate anion itself has almost ideal planar-trigonal symmetry, with C–O distances of 1.28(2)–1.28(6) Å). The principal orientation of the carbonate anion in the β-modification still exists in the α-modification, except for the 24-fold disorder, which causes the oxygen positions to be smeared out. It is noteworthy that the "sphericity" created by the disorder is

© 2005 Wiley-VCH Verlag GmbH & Co. KGaA, Weinheim

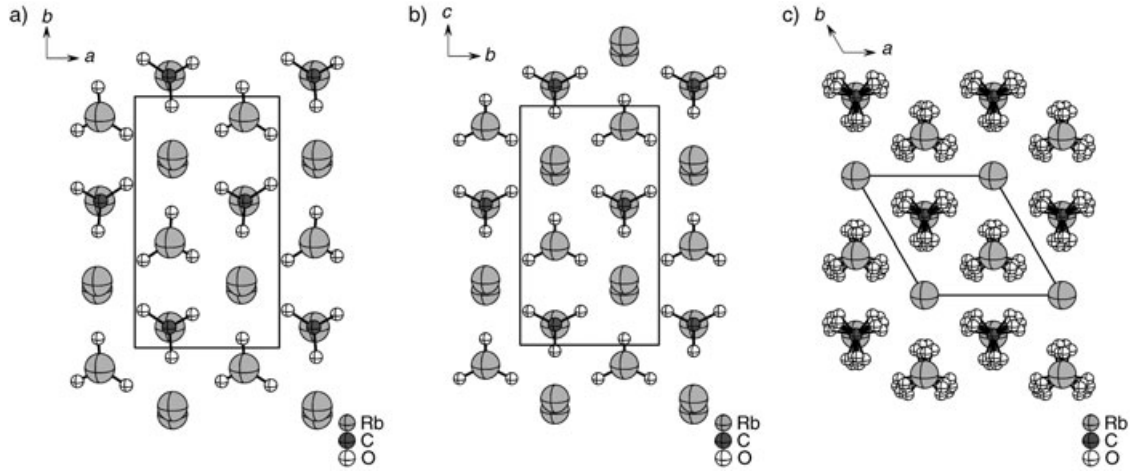

Figure 9. Ball-and-stick representation of the crystal structures of $Rb_2[CO_3]$: a) the monoclinic ($P2_1/c$) γ-phase at 385 K in a projection down the *c* axis; b) the orthorhombic (*Pnma*) β-phase at 734 K in a projection down the *b* axis; (c) the hexagonal ($P6_3/mmc$) α-phase at 860 K, showing the disorder of the carbonate anions, in a projection down the *c* axis.

much less pronounced for the carbonate phases than it is for the oxalate phases (Figure 8, Figure 9).

To get an easy access to the crystal structures and the topologies of the different high-temperature phases of the alkali-metal oxalates and carbonates, one can replace the oxalate or carbonate ions by a sphere at their center of gravity; that is, either the center between the C–C bond of the oxalate anion or the location of the carbon atoms in the case of the carbonate anion (Figure 10). As a general rule, all crystal structures of the alkali-metal oxalates and carbonates observed so far, at different temperatures, belong to the AlB_2 family (according to the definition used in the binary edition of the Pauling file[23]). The group–subgroup relationship for all anhydrous alkali-metal oxalates and carbonates, based on preliminary investigations[24] with the alkali-metal hyponitrites and some of the alkali-metal carbonates, is shown in Figure 11. Depending on the size of the cations and the anions, two idealized structure types occur within this family: the AlB_2 type (*P6/mmm*; anion at 0,0,0

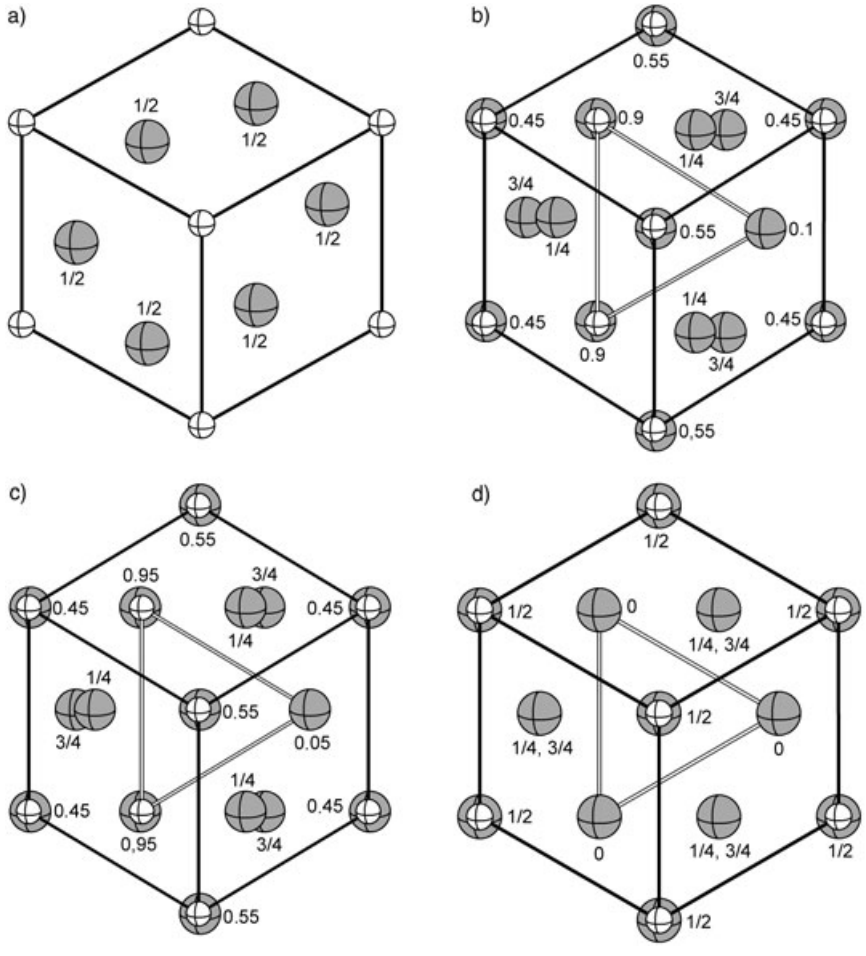

Figure 10. A comparison of the crystal packing of the δ- (*Pbam*, upper left), γ- ($P2_1/c$, upper right), β- (*Pnma*, lower left), and α-phase ($P6_3/mmc$, lower right) of potassium, rubidium, and cesium oxalate and carbonate in projections perpendicular to the (pseudo)-hexagonal layers of the anions. The center-of-gravity locations of the oxalate and carbonate anions (white balls) and the positions of the alkali-metal cations (gray balls) are drawn. The size of the balls was chosen for clarity. The fractional height of the cations is given. Solid lines connect anions at height 0, while hollow lines connect anions at height 1/2.

 © 2005 Wiley-VCH Verlag GmbH & Co. KGaA, Weinheim

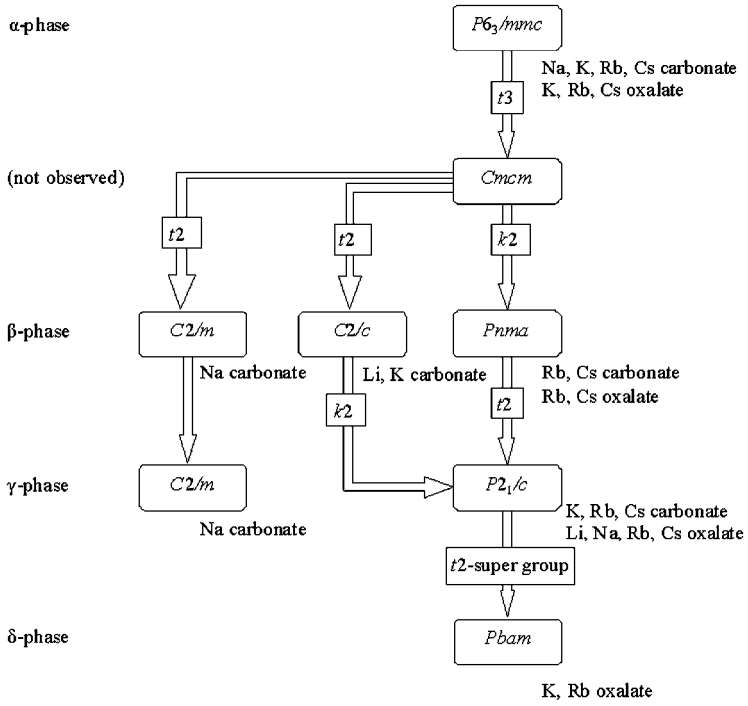

Figure 11. A lattice of observed crystallographic subgroups of all known room- and high-temperature phases of the alkali-metal oxalates and carbonates starting from the hexagonal close-packed archetype in $P6_3/mmc$ (t: Translationsgleich, k: Klassengleich).

and cation at 1/3,2/3,1/2) and the Ni_2In type ($P6_3/mmc$; anion at 2/3,1/3,1/4 and cations at 0,0,0 and 1/3,2/3,1/4). The hexagonal layers of the anions and the positions of the alkali-metal cations deviate from the idealized ones for all crystal structures in space groups other than those of the aristotypes. Furthermore, the degree of distortion with respect to the idealized structure types varies greatly with temperature, with the size and polarizability of the alkali-metal cations, and with the conformation and disorder of the anion.

In the layered AlB_2 type, the anions show a primitive hexagonal AAA (ph) packing and the two trigonal prismatic voids between two anionic layers are filled by the cations. In this way the trigonal prisms share all five faces with neighboring trigonal prisms, their three side faces within a layer, and their two base planes with consecutive layers. For the alkali-metal oxalates, this building principle is observed for $Li_2[C_2O_4]$ ($P2_1/c$), $Na_2[C_2O_4]$ ($P2_1/c$), δ-$K_2[C_2O_4]$ (*Pbam*), and δ-$Rb_2[C_2O_4]$ (*Pbam*) in order of decreasing distortion. The smaller the cation, the more it is shifted out of the center of the trigonal prisms. It appears that the oxalate anion must be in a flat conformation. As soon as the conformation of the oxalate anions changes to a staggered conformation, either static at lower temperature or disordered at higher temperature, the Ni_2In-type crystal structure is preferred. In case of the alkali-metal carbonates, only β-Li_2CO_3 ($C2/c$)[19,25] adopts a strongly distorted variant of the AlB_2 structure type. With increasing size of the cation the Ni_2In-type crystal structure is preferred.

In the Ni_2In type, the anions form a distorted hexagonal close-packing ABA (hcp) structure with half of the cations located in an octahedral void and the other half located in a trigonal bipyramidal void. The *c*/*a* relation strongly deviates from ideal hcp, thus distorting the octahedral voids to rhombic bipyramidal voids (Table 6). The structures may best be described by two interpenetrating frameworks of the two different anion polyhedra. The trigonal bipyramids are interconnected at the three corners of the trigonal base plane to form two-dimensional trigonal nets in the *ab* plane. Consecutive planes along the *c* direction are rotated by 180° around the *c* axis (6_3-screw axis). Thus, the three edges containing the vertex of each trigonal pyramid are shared between consecutive layers. The rhombic bipyramids are oriented in such a way that two trigonal faces, perpendicular to the *c* axis, are shared with rhombic bipyramids of neighboring layers. Within the *ab* plane, the rhombic bipyramids are connected by the six remaining edges to form a hexagonal net in projection. The voids between consecutive layers are filled by the trigonal bipyramids, which share all six faces with the rhombic bipyramids of two consecutive layers (three with each layer). In general, the degree of distortion decreases with increasing temperature (Figure 10). This structural feature is found for γ-$Na_2[CO_3]$ ($C2/m$), β-$Na_2[CO_3]$ ($C2/m$), α-$Na_2[CO_3]$ ($P6_3/mmc$), γ-$K_2[CO_3]$ ($P2_1/c$), β-$K_2[CO_3]$ ($C2/c$), α-$K_2[CO_3]$ ($P6_3/mmc$), γ-$Rb_2[CO_3]$ ($P2_1/c$), β-$Rb_2[CO_3]$ (*Pnma*), α-$Rb_2[CO_3]$ ($P6_3/mmc$), γ-$Cs_2[CO_3]$ ($P2_1/c$), β-$Cs_2[CO_3]$ (*Pnma*), α-$Cs_2[CO_3]$ ($P6_3/mmc$), α-$K_2[C_2O_4]$ ($P6_3/mmc$), γ-$Rb_2[C_2O_4]$ ($P2_1/c$), β-$Rb_2[C_2O_4]$ (*Pnma*), α-$Rb_2[C_2O_4]$ ($P6_3/mmc$), γ-$Cs_2[C_2O_4]$ ($P2_1/c$), β-$Cs_2[C_2O_4]$ (*Pnma*), and α-$Cs_2[C_2O_4]$ ($P6_3/mmc$).

Table 6. The deviation from ideal hexagonal packing (primitive hexagonal (ph) and hexagonal closed packed (hcp)) for the room- and high-temperature modifications of $Rb_2[C_2O_4]$.

$Rb_2[C_2O_4]$	Angle of the hexagonal mesh [°]	Inclination of hexagonal planes [°]	*c*/*a*
γ	114.4–122.6	8.4	1.26–1.32
β	117.8–121.0	3.0	1.24–1.25
α	120	0.0	1.27–1.31
ideal hcp	120	0.0	1.633
δ	119.1–121.7	0.0	0.561
ideal ph	120	0.0	1.0

© 2005 Wiley-VCH Verlag GmbH & Co. KGaA, Weinheim

Starting from the close-packed Ni_2In aristotype in space group $P6_3/mmc$, the subgroup relations of all observed space groups within the alkali-metal oxalate and carbonate series are given in Figure 10. The crystallographic relationships between the different crystal structures are best viewed in the projection of Figure 12. The matrices for transforming the unit-cell dimensions for the oxalate series are given, in 4×4 notation, by:

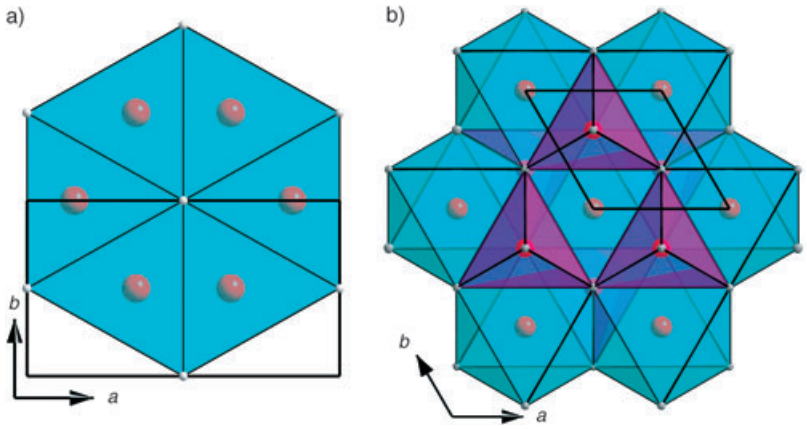

Figure 12. A packing diagram of the crystal structures of δ-$K_2[C_2O_4]$ at 295 K (*Pbam*) and α-$K_2[C_2O_4]$ at 752 K as projections down the *c*-axis giving only the center-of-gravity locations for the oxalate anion. The idealized AlB_2 (left) and Ni_2In (right) structure types are clearly visible.

$$Pbam \xrightarrow{\begin{bmatrix}0&0&2&0\\1&0&0&0\\0&1&0&0\\0&0&0&1\end{bmatrix}} P\frac{2_1}{c} \xrightarrow{\begin{bmatrix}0&0&1&0\\1&0&0&0\\0&1&0&0\\0&0&0&1\end{bmatrix}} Pnma \xrightarrow{\begin{bmatrix}0&-1/2&-1/2&1/4\\0&1&0&1/4\\1&0&0&1/4\\0&0&0&1\end{bmatrix}} P\frac{6_3}{m}mc$$

Further evidence for the general underlying packing principle of the alkali-metal oxalate and carbonate phases is given by the fact that, for the heavier alkali metals rubidium and cesium, the sequence of phase transitions from the γ- via the β- to the α-phase, as well as their crystal structures, are the same for the oxalates and the carbonates.

Thus, the sequence of high-temperature phase transitions of the alkali-metal oxalates and carbonates can best be understood from geometrical and energetic considerations. The disorder of the oxalate and carbonate groups at high temperatures provides significant entropic stabilization of the high-temperature phases relative to the low-temperature ordered structures. It has been shown that the alkali-metal oxalates and carbonates tend towards hexagonal close-packed crystal structures, and that the different phases are mainly distinguished by changes in the anionic packing. The driving force for the structural phase-transitions is clearly related to the steric requirements of the anions, which change due to the increasing dynamics at higher temperature. Interestingly, the "sphericity" of the anions, either static or dynamic, is more important than the actual radius of the "spheres".

Conclusion

A comprehensive study of the potassium, rubidium, and cesium oxalates with respect to their behavior at elevated temperatures has revealed a surprisingly uniform structural evolution of all three representatives. All crystal structures of the alkali-metal oxalates can be reduced to two basic structure types, the AlB_2 and the Ni_2In type, by substituting the alkali-metal cations for boron or nickel, and the barycenters of the oxalate anions for aluminum or indium. This holds true for all high-temperature modifications as well. With the exception of the δ→γ transitions, all transitions are driven by the onset or enhancement of dynamical rotational disorder of the anions. Despite the different shapes of the oxalate and carbonate anions, both families of alkali-metal salts exhibit the same basic structural features. As a general tendency, the Ni_2In arrangement gains preference over the AlB_2 packing type with increasing temperature and increasing effective radius of the cations. From the structural observations, convincing evidence can be derived that the process of thermal degradation of the alkali-metal oxalates to their carbonates is topochemical in nature.

Experimental Section

Preparation: Potassium, rubidium, and cesium oxalate were prepared by dehydration of the corresponding monohydrates for 18 h at a temperature of 373 K under vacuum. Potassium oxalate monohydrate was used as purchased ($K_2[C_2O_4]\cdot H_2O$, Fluka, puriss. p. a.). Rubidium and cesium oxalate monohydrate were synthesized by treatment of the corresponding carbonates ($Rb_2[CO_3]$, Alfa Aesar, p. a.; $Cs_2[CO_3]$, Chempur, p. a.) with oxalic acid dihydrate ($H_2[C_2O_4]\cdot 2H_2O$, Fluka, puriss. p. a.) in an aqueous solution. The solution was stirred for 12 h at 353 K, and the water was subsequently removed by distillation. The precipitates were washed with diethyl ether and acetone. The dehydrated oxalates were handled under argon to prevent any possible contamination with water.

Thermal analysis: Thermal analyses of potassium, rubidium, and cesium oxalate were conducted using DSC as well as simultaneous DTA/TGA/MS techniques. DSC measurements were carried out with a DSC 404 calorimeter (Netzsch, Selb) at a heating rate of 5 K min^{-1} in vacuum with the samples sealed in aluminum boxes. For DTA/TGA/MS investigations a Simultaneous-Thermal-Analysator STA 409 (Netzsch, Selb) was used, with the samples in alumina crucibles in an argon flow of 100 mL min^{-1} at a heating rate of 10 K min^{-1}. All temperatures given are the onset values of the corresponding peak. While for the phase-transition temper-

 © 2005 Wiley-VCH Verlag GmbH & Co. KGaA, Weinheim

ature the DSC data were analyzed, the DTA/TGA data were used for the decomposition.

Powder diffraction: In situ X-ray powder-diffraction data of potassium, rubidium, and cesium oxalate at high temperature were collected in transmission geometry with a hot, small-environment cell for real-time studies on a motorized goniometer head at beamline X7B at the National Synchrotron Light Source (NSLS) at Brookhaven National Laboratory. X-rays of energy 13.5 keV were selected by a double flat-crystal monochromator in ultra-high vacuum located 8 m from the source. The X-ray beam was focused vertically by a spherical, rhodium-coated, silicon carbide mirror located 5 m from the source and horizontally by a cylindrical aluminum mirror with nickel plating coated by rhodium located 13 m from the source. The size of the beam was adjusted to a height of approximately 0.5 mm and a width of 2 mm. As detector, a MAR 345 image-plate reader was set up perpendicular to the beam path at a distance of approximately 170 mm from the sample. LaB_6 was used as an external standard to determine the beam center, sample-to-detector distance, exact wavelength, and tilting angle of the image plate. The samples were contained in sealed quartz capillaries with diameters between 0.3 and 0.5 mm loaded in a sapphire tube of 0.8 mm diameter attached to a flow-reaction cell.[26,27] The temperature was monitored and controlled by a 0.01 in thermocouple (Omega) which was inserted straight into the sapphire tube adjacent to, and in contact with, the sample capillary. The sample was aligned such that the sample closest to the thermocouple was in the X-ray beam path. The samples were heated in the temperature range from room temperature up to 900 K by a small resistance heater wrapped around the sapphire tube. During exposure, the samples were rocked for several degrees in order to improve randomization of the crystallites. Exposure times of between 30 s and 1 min were chosen depending on the saturation intensity of the image plate. Integration of the full-circle powder patterns was performed using the program FIT2D[28,29] to give diagrams of corrected intensities versus the scattering angle 2θ (Figure 6). Reflections due to the single-crystal sapphire capillary were excluded. We observed that the diffracted intensity was quite uniformly distributed over the Debye–Scherrer rings, thereby ruling out severe grain-size effects and preferred orientation. Low-angle diffraction peaks had a typical FWHM of 0.15° 2θ. Further experimental details can be found in Table 5.

Data reduction on all powder-diffraction patterns was performed using the GUFI program.[30] Several previously unknown high-temperature phases of the alkali-metal oxalates and their decomposition products (carbonates) were detected. The observed phases were named according to Table 2. Indexing of all previously unknown high-temperature phases with ITO[31] led to the lattice parameters given in Table 3 and Table 4. The number of formula units per unit cell could be determined from volume increments. The extinctions found in the powder patterns indicated *P6₃/mmc* for α-$K_2[C_2O_4]$, α-$Rb_2[C_2O_4]$, α-$Rb_2[CO_3]$, α-$Cs_2[C_2O_4]$, and α-$Cs_2[CO_3]$, and *Pnma* for β-$Rb_2[C_2O_4]$, β-$Rb_2[CO_3]$, β-$Cs_2[C_2O_4]$, and β-$Cs_2[CO_3]$ as the most probable space groups; these were later confirmed by Rietveld refinements. The peak profiles and precise lattice parameters were determined by LeBail-type fits[32] using the programs GSAS[33] and FULLPROF.[34,35] The background was either modeled manually with GUFI or by using orthogonal Chebyshev polynomials up to order 15 as implemented in GSAS. The peak-profile was described by a pseudo-Voigt function in combination with a special function that accounts for the asymmetry due to axial divergence.[36,37] The powder patterns of the β-phases in *Pnma* exhibit anisotropic peak broadening, which is mainly caused by lattice strain and could be modeled by the phenomenological strain model of Stephens,[38] using six parameters, as implemented in GSAS.

All previously unknown crystal structures were solved using the DASH structure-solution package.[39] The measured powder patterns were subjected to a Pawley refinement[40] in space groups *P6₃/mmc* for the α-phases and space group *Pnma* for the β-phases in order to extract correlated integrated intensities from the pattern. Good fits to the data were obtained. An internal coordinate description of the oxalate and carbonate moieties was constructed using bond lengths, angles, and torsion angles (in the case of the oxalate anion) from corresponding alkali-metal oxalate and carbonate phases.[9] The torsion angle between the two carboxylate groups of the oxalate anion could not be assigned a precise value in advance, and was thus treated as an internal degree of freedom in the simulated annealing procedure. The positions of the two crystallographically independent alkali-metal cations, as well as the position, orientation, and conformation of the oxalate and carbonate anions in the unit cell, were postulated and the trial structure was subjected to a global optimization in direct space using DASH. The structure giving the best fit to the data was validated by Rietveld refinement[41] of the fractional coordinates obtained at the end of the simulated annealing run.

With respect to the lower data quality, only LeBail-type fits could be performed for the different phases of cesium carbonate, but the similarity of the powder patterns to those of the rubidium carbonate phases led us to the conclusion that the α-, β-, and γ-phases of $Rb_2[CO_3]$ and $Cs_2[CO_3]$ are isostructural.

Rigid-body Rietveld refinements (Figure 7) were performed on all powder patterns of $K_2[C_2O_4]$ (α- and δ-modification), $Rb_2[C_2O_4]$ (α, β, γ, and δ), $Cs_2[C_2O_4]$ (β, γ, and δ), and α-$K_2[CO_3]$ and $Rb_2[CO_3]$ (α, β, and γ). The unit-cell parameters, the background, and the peak profile were taken from the corresponding LeBail fits. The strong (presumably) dynamic disorder of the high-temperature phases of the alkali-metal oxalates and carbonates was modeled depending on the quality of the powder-diffraction patterns by rigid-body TLS refinement and/or by split positions according to space-group symmetry (up to 24-fold for *P6₃/mmc*). Agreement factors (*R* values) are listed in Table 3 and Table 4, and the coordinates are given in the Supporting Information. The intramolecular distances were fixed within the rigid bodies and are not discussed. Due to the disorder, the packing is discussed on the basis of the center of gravity locations of the oxalate and carbonate anions.

Further details of the crystal-structure investigation of the alkali-metal carbonates can be obtained from the Fachinformationszentrum Karlsruhe, 76344 Eggenstein-Leopoldshafen, Germany, (fax: (+49) 7247-808-666; e-mail: crysdata@fiz.karlsruhe.de on quoting the depository numbers CSD-414120 (α-$K_2[CO_3]$), CSD-414121 (α-$Rb_2[CO_3]$), CSD-414122 (β-$Rb_2[CO_3]$), and CSD-414123 (γ-$Rb_2[CO_3]$).

CCDC-241896 (α-$K_2[C_2O_4]$), CCDC-241897 [δ-$K_2[C_2O_4]$), CCDC-241898 [α-$Rb_2[C_2O_4]$), CCDC-241899 (β-$Rb_2[C_2O_4]$), CCDC-241893 (γ-$Rb_2[C_2O_4]$), CCDC-241900 (δ-$Rb_2[C_2O_4]$), CCDC-241901 (α-$Cs_2[C_2O_4]$), CCDC-241894 (β-$Cs_2[C_2O_4]$), and CCDC-214895 (γ-$Cs_2[C_2O_4]$) contain a part of the supplementary crystallographic data for this paper. These data can be obtained free of charge from The Cambridge Crystallographic Data Centre via www.ccdc.cam.ac.uk/data_request/cif.

Acknowledgement

We thank Dr. Christian P. M. Oberndorfer and Ing. Klaus Hertel for conducting the DTA/TGA/MS and the DSC measurements. The synchrotron measurements were carried out in part at the National Synchrotron Light Source at Brookhaven National Laboratory, which is supported under contract DE-AC02-98CH10886 by the US Department of Energy, Division of Chemical Sciences, Office of Basic and Energy Sciences. Financial support by the Max-Planck Society (MPG), the Bundesministerium für Bildung und Forschung (BMBF) and the Fonds der Chemischen Industrie (FCI) is gratefully acknowledged.

[1] A. J. P. Andrade, A. J. S. Machado, *Mater. Lett.* **1992**, *13*, 96–101.
[2] F. H. Cheng, T. Y. Tseng, *J. Am. Ceram. Soc.* **1990**, *73*, 889–892.
[3] S. Bhattacharjee, M. K. Paria, H. S. Maiti, *Mater. Lett.* **1992**, *13*, 130–134.
[4] T. T. Fang, H. B. Lin, *J. Am. Ceram. Soc.* **1989**, *72*, 1899–1906.
[5] M. J. Munson, R. E. Riman, *J. Therm. Anal.* **1991**, *37*, 2555–2566.
[6] B. Beagley, R. W. H. Small, *Acta Crystallogr.* **1964**, *17*, 783–788.
[7] G. A. Jeffrey, G. S. Parry, *J. Am. Chem. Soc.* **1954**, *76*, 5283–5286.

© 2005 Wiley-VCH Verlag GmbH & Co. KGaA, Weinheim

[8] D. A. Reed, M. M. Olmstead, *Acta Crystallogr. Sect. B* **1981**, *37*, 938–939.
[9] R. E. Dinnebier, S. Vensky, M. Panthöfer, M. Jansen, *Inorg. Chem.* **2003**, *42*, 1499–1507.
[10] D. Dollimore, D. Tinsley, *J. Chem. Soc. A* **1971**, 3043–3047.
[11] T. Higashiyama, S. Hasegawa, *Bull. Chem. Soc. Jpn.* **1971**, *44*, 1727–1730.
[12] Y. Masuda, R. Ito, T. Matsuda, Y. Ito, *Thermochim. Acta* **1988**, *131*, 291–296.
[13] I. A. Kahwa, A. M. Mulokozi, *J. Therm. Anal.* **1981**, *22*, 61–65.
[14] R. Ito, Y. Masuda, Y. Ito, *Thermochim. Acta* **1988**, *127*, 159–170.
[15] D. Dollimore, *Thermochim. Acta* **1987**, *117*, 331–363.
[16] D. Dollimore, *Thermochim. Acta* **1991**, *177*, 59–75.
[17] A. K. Galwey, M. E. Brown, *Thermal Decomposition of Inorganic Solids, Ch. 16*, Elsevier, Amsterdam, **1999**.
[18] A. K. Galwey, M. A. Mohamed, *J. Chem. Soc. Faraday Trans. 1* **1985**, *81*, 2503.
[19] Y. Idemoto, J. W. J. Ricardson, N. Koura, S. Kohara, C.-K. Loong, *J. Phys. Chem. Solids* **1998**, *59*, 363–376.
[20] B. M. Gatehouse, D. J. Lloyd, *J. Chem. Soc. Dalton Trans.* **1972**, 70–72.
[21] H. Y. Becht, R. Struikmans, *Acta Crystallogr. Sect. B* **1976**, *32*, 3344–3346.
[22] H. Ehrhardt, H. Schweer, H. Seidel, *Z. Anorg. Allg. Chem.* **1980**, *462*, 185–198.
[23] *Pauling Files Binaries Edition*, Vers. 1.0, Release 2002/1, Material Phases Data System, Vitznau, and Crystal Impact, Bonn.
[24] C. Feldmann, M. Jansen, *Z. Kristallogr.* **2000**, *215*, 343–345.
[25] J. Zemann, *Acta Crystallogr.* **1957**, *10*, 664–666.
[26] J. B. Parise, C. L. Cahill, Y. J. Lee, *Can. Mineral.* **2000**, *38*, 777–800.
[27] P. J. Chupas, M. F. Circolo, J. C. Hanson, C. P. Grey, *J. Am. Chem. Soc.* **2001**, *123*, 1694–1702.
[28] A. P. Hammersley, *FIT2D*, Vers. 9.129, ESRF Internal Report ESRF98 A01T.
[29] A. P. Hammersley, S. O. Svenson, M. Hanfland, D. Hauserman, *High Pressure Res.* **1996**, *14*, 235–248.
[30] R. E. Dinnebier, L. Finger, *Z. Kristallogr.* **1998**, *Supplement to Issue 15*, 148.
[31] J. W. Visser, *J. Appl. Crystallogr.* **1969**, *2*, 89–95.
[32] A. Le Bail, H. Duroy, J. L. Fourquet, *Mater. Res. Bull.* **1988**, *23*, 447–452.
[33] A. C. Larson, R. B. von Dreele, *GSAS*, Vers. 2002, Los Alamos National Laboratory Report LAUR 86–748, Los Alamos, USA.
[34] J. Rodriguez-Carvajal, *Abstracts of the Satellite Meeting on Powder Diffraction of the XV Congress of the IUCr*, p. 127, Toulouse, France, **1990**.
[35] J. Rodriguez-Carvajal, *FULLPROF.2k*, Version 1.9c, Laboratoire Leon Brillouin, Gif-sur-Yvette, France, **2001**.
[36] P. Thompson, D. E. Cox, J. B. Hastings, *J. Appl. Crystallogr.* **1987**, *20*, 79–83.
[37] L. W. Finger, D. E. Cox, A. P. Jephcoat, *J. Appl. Crystallogr.* **1994**, *27*, 892–900.
[38] P. W. Stephens, *J. Appl. Crystallogr.* **1999**, *32*, 281–289.
[39] W. I. F. David, K. Shankland, N. Shankland, *Chem. Commun.* **1998**, 931–932.
[40] G. S. Pawley, *J. Appl. Crystallogr.* **1981**, *14*, 357–361.
[41] H. M. Rietveld, *J. Appl. Crystallogr.* **1969**, *2*, 65–71.
[42] B. Hinrichsen, R. E. Dinnebier, M. Jansen, *Abstracts of the EPDIC IX conference*, Prague, Czech Republic, **2004**, 82–83.

Received: June 18, 2004
Published online: December 29, 2004

 © 2005 Wiley-VCH Verlag GmbH & Co. KGaA, Weinheim